CHAPTER 2

Precession Instrumentation

Precession is a tool designed to improve the quality of diffraction data from the TEM. Consequently, developing effective instrumentation and protocols is critical to the quality and reliability of results. In this chapter, the requirements and underlying principles for obtaining high-quality precession patterns are described. The principles and methods described in this chapter are embodied in the real-world implementations presented in appendices B and C; appendix D presents a third-generation precession instrument that is currently being constructed. Appendix A contains background information for understanding the implementation details for readers who are unfamiliar with electronics. Finally, appendix E contains general procedures for aligning the family of precession systems presented here to obtain high-quality precession patterns. The contents of this chapter and some of the referenced appendices are reproduced from Own et al. (2005a) and Own and Marks (2005a). Details are also contained within US patent application number 60/531,641, filed December 2004 (Own and Marks 2004).

Considerable testing and validation is necessary before a new technique can become widely accepted. An obstacle to this is the inherent scarcity of equipment in the field on which to test and understand experimental parameters, and development of a common language to describe them. At the start of this work in 2000, there were two known precession instruments based upon the Philips EM430 and Philips CM30/T microscopes (Vincent and Midgley 1994; Gemmi 2001). The early precession studies using these instruments have described experiments and compared precession to conventional methods (refer to section 1.4.1), but only cursory information has been given about implementation of the precession devices used. Additionally, these investigations have not described experiment parameters in detail. It is now apparent that experiment geometry is critical to the behavior of the resulting dataset (Own and Marks 2005b; Own et al. 2005b), thus a comprehensive set of variables including cone semiangle, convergence, probe size, and specimen image stability should necessarily accompany such studies.

It is convenient to first define some general language for precession. Tilt before the specimen is referred to as BT (beam tilt) and the synchronous de-tilt below the specimen is called DS (descan). In this chapter, precession electron diffraction patterns will be referred to as "precessed DP's" while conventional selected-area or focused-probe diffraction patterns will simply be called "DP's".

2.1. Precession Geometry

Precession electron diffraction is in principle equivalent to the X-ray Buerger precession camera. However, instead of precessing the crystal and detector, the beam itself is precessed synchronously prior to and after interaction with the specimen. The geometry is straightforwardly demonstrated using schematic pictures. Figure 1.10 from chapter 1 describes the principle most simply: the incident beam is tilted before the specimen and the diffracted beams are synchronously de-tilted after the specimen and measured at the diffraction plane. To understand the experiment parameters, it is necessary to examine this process in detail in reciprocal space.

In the kinematical description, the electron probe, which has wavelength λ much smaller than the atomic spacings, is similarly represented in reciprocal space by the wavevector $\mathbf{k}_0$, where $|\mathbf{k}_0| = 1/\lambda$. The electron probe interacts with the crystal and is scattered by the periodic atoms within the structure with amplitude $\phi_{\mathbf{g}}$, given by

$$\phi_{\mathbf{g}} = \sum_{n=1}^{N} F_n e^{-2\pi i \mathbf{k}.\mathbf{r}_n}, \tag{2.1}$$

where F_n is the scattering factor from unit cell n and N is the number of unit cells. The scattering from a periodic lattice of atoms in real space therefore gives rise to a reciprocal lattice, representing spatial frequencies within the real structure. In other words, possible excitations (where Bragg's law, equation 1.14, is satisfied) are described by the intersection of a sphere of radius $|\mathbf{k}|$ with the reciprocal lattice. This is the well-known Ewald construction, and the sphere describing possible excitations is called the Ewald sphere. Mathematically, the excited reflection vector is defined as $\mathbf{g} = \mathbf{k}_0 - \mathbf{k}_{\mathbf{g}} - \mathbf{s}_{\mathbf{g}}$, where $|\mathbf{k}_0| = |\mathbf{k}_{\mathbf{g}}|$, and $|\mathbf{k}_{\mathbf{g}}| \gg |\mathbf{g}|$, and $\mathbf{s}_{\mathbf{g}}$ is a quantity called *excitation error* which will be defined shortly. For 200 kV electrons, $|\mathbf{k}_0| \approx 40$ Å^{-1}.

In electron diffraction, scattering from the crystal can occur when Bragg's law is not perfectly met. The deviation from the point of perfect intersection signifying the Bragg condition is quantified by the *excitation error*, $\mathbf{s}_{\mathbf{g}}$. The scattering can be approximated by an integral,

$$\phi_{\mathbf{g}} = \frac{F_g}{V_c} \int_{crystal} e^{-2\pi i \mathbf{k}.\mathbf{r}} d\mathbf{r}, \tag{2.2}$$

where V_c is the volume of the unit cell. This is the Fourier transform of the crystal. In TEM, the crystal is thin in the z direction but large in the x and y directions, so by the Fourier transform relationship, the reciprocal lattice points are finite shapes (the shape function) elongated distinctly in the z-axis (relrods):

$$\phi_{\mathbf{g}} = \frac{F_g}{V_c} \int_0^A \int_0^B \int_0^C e^{-2\pi i \mathbf{k}.\mathbf{r}} dx dy dz, \tag{2.3}$$

where A, B, and C are crystal dimensions in the x, y, and z axes, respectively. Excitation of a relrod can thus occur when the Ewald sphere does not intersect the reciprocal lattice point exactly, and in kinematical theory the intensity scattered into reflection $k_{\mathbf{g}}$ is directly related to the shape of the relrod that represents $\mathbf{g}$. Following from the Fourier inversion of the top hat function that represents, in the z-axis, the flat crystal bounded on both sides by vacuum, the shape function is the sinc function:

$$|\phi_{\mathbf{g}}| \approx \frac{F_g}{V_c} \frac{\sin \pi A u}{\pi u}, \tag{2.4}$$

where u is the component of $\mathbf{s_g}$ along the z direction. The thicker the specimen, the smaller the oscillation periodicity of the shape function and the more peaked about $u = 0$. The set of all excited reflections projected along the z-axis onto the x-y plane forms the diffraction pattern.

The configuration of the Ewald construction relevant to PED is depicted in figure 2.1. The BT operation in precession is equivalent to rocking the Ewald sphere about a pivot point corresponding to the forward-scattered reflection (origin) of the zeroth-order Laue zone (ZOLZ). For the moment, ignore convergence (α) and consider only the dashed lines in the figure. In the snapshot represented by figure 2.1(a) where $\theta = 2n\pi$ and cone semi-angle is at fixed ϕ, reflection $\mathbf{g}$ — whose intensity is shown schematically on the right as a vertically-oriented sinc function — is excited with a moderate positive excitation error $\mathbf{s_g}$. Reflections near $x = R_0$ exhibit maximum $\mathbf{s_g}$, and reflections at $2R_0$ have $\mathbf{s_g} = 0$. Beyond $2R_0$, $\mathbf{s_g}$ becomes negative and decreases monotonically with increasing spatial frequency. In the x-y plane, the intersection of the Ewald sphere with the ZOLZ describes a circle of illuminated reflections tangent to the origin as shown in figure 2.1(b). The reflections with most positive $\mathbf{s_g}$ are at the center of this circle.

In real-world experiments, the beam usually has a finite convergence angle α, and sometimes PED is operated with a convergent beam mode where α is relatively large. When the convergence angle is non-zero, a segment of the shape function describing reflection $\mathbf{g}$ becomes simultaneously excited, where the sampling range along the z-direction depends upon the convergence angle α as shown by the solid lines in figure 2.1(a). In the limit of parallel illumination, $\alpha \to 0$. The parallel illumination configuration is used for the systems presented in this thesis.

During precession, the tilted beam precesses about the z-axis tracing out a circuit of $\theta = [0, 2\pi]$. The important point is that, at any given θ along the precession, few reflections are simultaneously excited. Typically only one reflection will be strongly excited and the other excitations along the ZOLZ ring are only weakly coupled because systematic re-diffraction paths are not simultaneously active. In terms of the intensity collected, the sphere intersects each reflection in reciprocal space through a range of excitation errors $\mathbf{s}_g$ and spends very little time during the exposure dwelling in any particular multiply-excited condition where dynamical effects may be prominent.

The intensity is integrated at the detector (conjugate with the diffraction plane) by taking a time-resolved measurement over an integral multiple of the revolution period. In practice, the

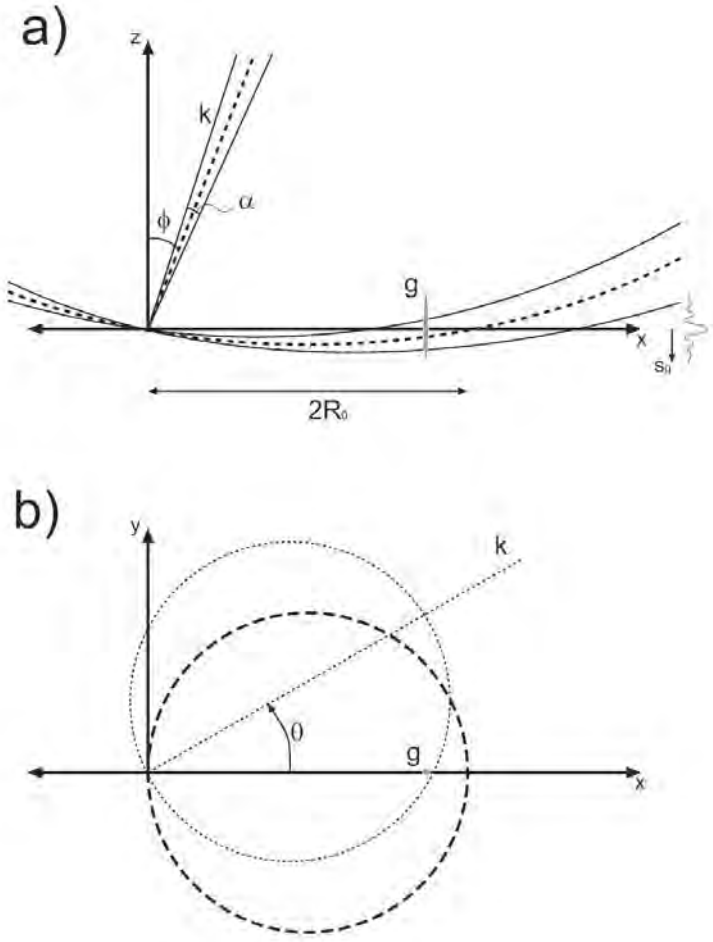

Figure 2.1. Reciprocal space geometry in (a) $x - y$ plane and (b) $x - z$ plane. The beam precesses about the z-axis maintaining constant ϕ. In (b), the ZOLZ (bold dashed circle) precesses about the z-axis.

exposure time is not synchronous to the precession, therefore the precession is run very rapidly (≈ 60 Hz) to ensure complete integration. Figure 2.2 demonstrates the integration process using simulated [010] patterns of a $(Ga,In)_2SnO_4$ crystal of 412 Å thickness (the real space analog to figure 2.2 is figure C.4 in the appendix). Amplitude patterns are used to more clearly portray the Laue circle. Figure 2.2(a) shows eight discrete tilts along the precession circuit described by θ, each tilted by $\phi = 24$ mrad. In each snapshot, usually only one reflection is strongly excited. The most prominent dynamical effects are systematic rediffraction paths which are excited only along the Laue circle and tangent to the transmitted beam. A given systematic path is excited only momentarily during the precession twice and is limited in extent — the maximum index of multiply-excited systematic reflections — by the curvature of the Laue circle. The center

image is the precessed DP, representing a sum of the amplitudes of 1000 discrete tilts. Figure 2.2(b) is the simulated pattern of the conventional DP for the same thickness. The difference between the two patterns is readily apparent, and analyses in the next chapter will show the intensities in (a) are much more kinematical than (b).

As pointed out in section 1.4, PED is similar to powder and lamellar texture diffraction, which operate on a similar principle of integration over excitation error by crystal rotation. However, there are some important differences. Powder diffraction integrates the excitation error over all of reciprocal space, and texture patterns integrate excitation error only about a small cone of axes with average axis direction perpendicular to the incident beam. The symmetry is completely lost in powder patterns and is often compromised in texture patterns along one axis, whereas the full symmetry of the ZAP is preserved in PED. Another difference is that the thickness of the crystal is often more controlled in PED than in the polycrystal diffraction methods. This arises because the fine probe in PED illuminates a smaller specimen region (reducing the possibility for large thickness variation), and because polycrystal diffraction is subject to crystallite size distribution and morphology within the specimen — experimental variables that are difficult to control.

PED using higher beam tilt angles more closely approximates powder diffraction and, as shall be seen in later chapters, the intensities become more kinematical with increasing ϕ. Electron optical limitations limit the highest angle possible in the instrument, however, the structure itself also affects the maximum targeted semi-angle due to first-order (FOLZ) and zoroth-order Laue zone (ZOLZ) overlap. Figure 2.3(a) demonstrates this limitation: during precession the FOLZ point closest to the precession axis, defined by point F, is revolved to the opposite side of the projection axis during precession (indicated by F'). If F' lies directly above a ZOLZ reflection and has considerable scattering intensity, the zeroth-order reflection intensity will be obfuscated and must be excluded from the dataset. This excludes structures where the HOLZ are easily distinguishable from the ZOLZ, but for unknown structures this analysis applies unequivocally. The usable radius of the diffraction pattern is described by the relationship

$$\gamma = \arccos\left(\frac{k\cos(\phi) - \frac{1}{c}}{k}\right) - \phi, \tag{2.5}$$

where ϕ is the cone semi-angle, c is the projection-axis unit cell dimension or repeat distance along the beam direction, $\mathbf{k}$ is the wavevector, and γ is — by the small-angle approximation — the approximate usable DP radius in radians.

Figure 2.3(b) shows the unit cell dimension c plotted against γ for four different cone semi-angles, showing the rapid decrease in usable DP radius as unit cell dimension increases. For reference, $\gamma = 25$ mrad corresponds to ≈ 1 Å^{-1} at 200 kV. Increasing ϕ also increases the Laue zone overlap constraint — in the worst case, investigating a large unit cell structure of 25 Å in the projected direction will yield very little trustworthy diffraction information when $\phi > 50$ is

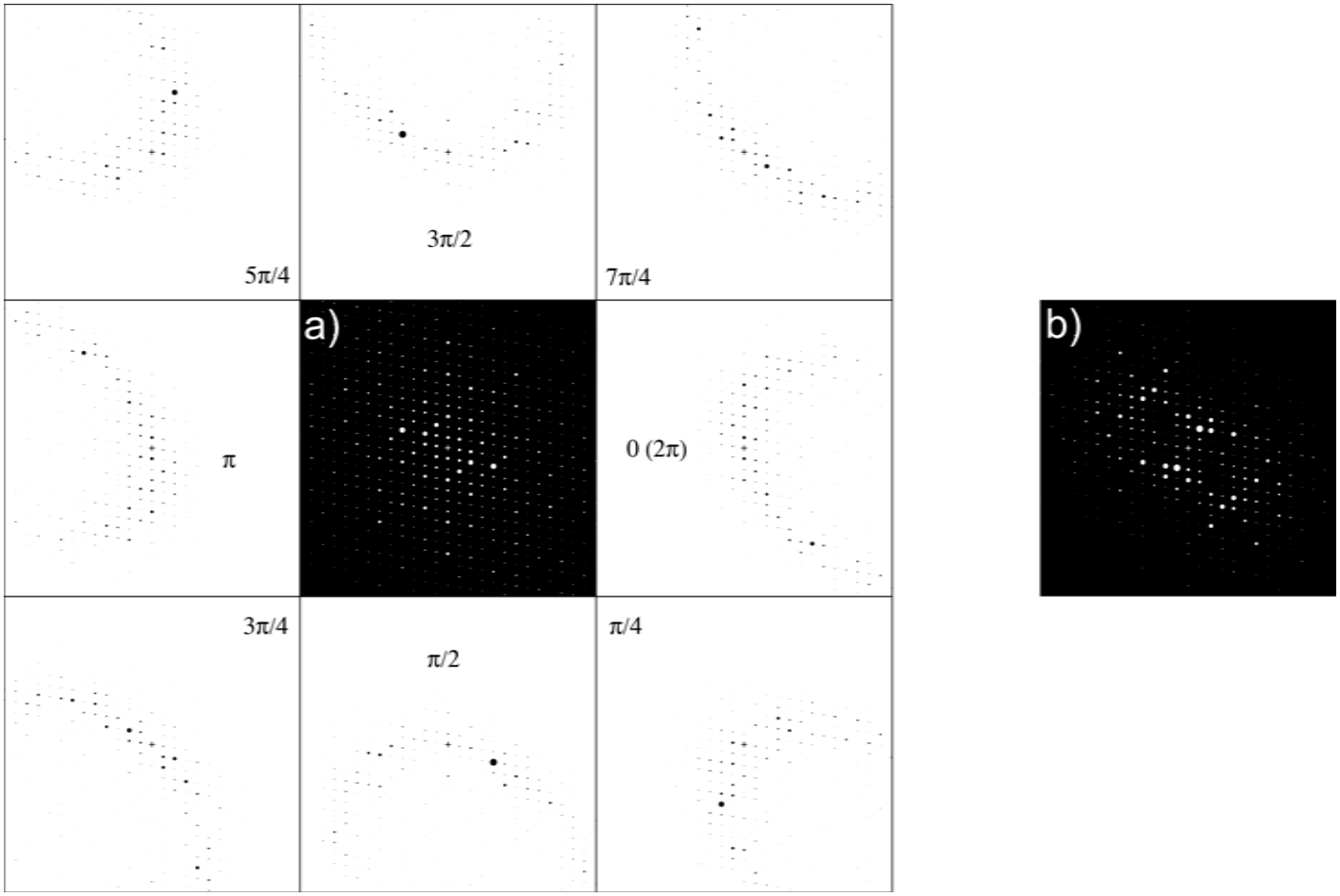

Figure 2.2. Center precession pattern (a) is an integration of the simulated tilt series (contrast inverted) that surrounds it forming an effective cone of illumination. (b) is the non-precessed pattern. t = 41nm, ϕ = 24mrad, patterns represent structure factor amplitudes.

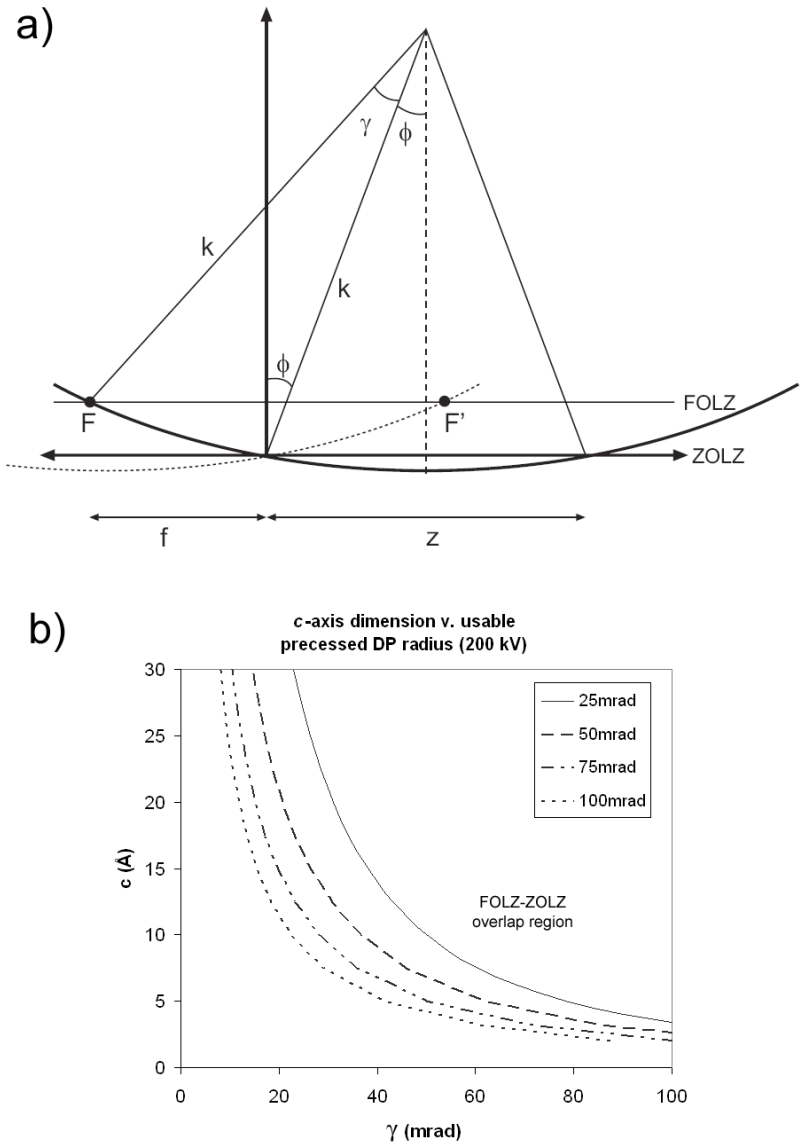

Figure 2.3. a) Precession geometry schematic showing the relationship between ZOLZ and FOLZ excitations. The distance z corresponds to the zero order zone radius; γ corresponds to the usable diffraction radius in mrad. b) Plot of unit cell dimension against usable diffraction radius γ for various cone semi-angles. The lines describe γ, which decreases with ϕ and specimen unit cell thickness.

used (recall that the number of reflections increases roughly with the square of $|\mathbf{g}|$). While it is desirable to harvest reflections to as high of resolution as possible, the most important spots for Direct Methods are those within an annulus containing key information about interatomic distances (Sinkler et al. 1998b). To generate a good initial starting structure model, Direct

Methods should have reflections to roughly 1 $Å^{-1}$, corresponding to $\gamma \approx$ 25-30 mrad at 200 kV. For this reason, structures or projections for wich $c > 15$ Å will be difficult to work with at large ϕ due to FOLZ overlap, while structures with $c < 10$ Å are very amenable. Higher energy is advantageous here because the Ewald sphere is flatter for smaller λ.

PED will be most amenable for certain zones of plate-like structures, where the projection normal to the cleavage plane results in a small repeat distance along the beam direction. The GITO structure is a good example: the projection-axis dimension $c = 3.17$. According to equation 2.5, GITO yields a usable DP radius (γ) of 100 mrad when $\phi = 24$mrad, and this decreases to about $\gamma = 60$ mrad (quite ample) when $\phi = 100$ mrad. It should be noted that the ZOLZ reflections can potentially be recovered if a partial scan ($\theta = [0, \pi]$ radians) is used. The logical extension of this is a data mining approach where discrete tilts are acquired independently and the spots integrated in software rather than within a single exposure. This approach is rather complex in terms of implementation but very powerful, and some discussion will be reserved in chapter 6 for this topic.

2.2. Retrofit Requirements

Nearly any TEM can be retrofitted for precession diffraction. The electron beam path must be altered at some point in the microscope by a physical deflector system, so a location will always be available at which analog signals from the precession system can be inserted. An exception would be the case of digital power amplifiers, however, it is extremely unlikely that such amplifiers would be used in high current applications like coil drivers due to switching noise. The scheme that will be described in the following sections is therefore applicable to both digitally-controlled microscopes and older analog instruments.

Practically, the microscope must be equipped to acquire both images and diffraction patterns from a specimen. A double-tilt goniometer stage is required, as is mechanical specimen height adjustment. In terms of the optics, the microscope should be able to form a fine probe and spherical aberration should be relatively low to ensure good probe localization. Pre-specimen optics must support a tilt angle of at least 25 mrad. De-scan is best accomplished in immediately-post-specimen deflectors if available, and if not, intermediate lens deflectors with sufficient range are desirable. The least desirable location for de-scan is at the projector deflector since the camera length cannot be changed without losing alignment. Almost all microscopes include the image shift feature, and the image deflector without exception can support large deflection amplitude, so this location would likely be most commonly used for de-scan in older instruments.

An important requirement is a detector with a sufficient dynamic range from which measurements can be acquired. Electron-sensitive film is very common but has a dynamic range of only about 10^2. An exposure scaling system is discussed in appendix F that can be used to obtain intensities with very high dynamic range (4 or 5 orders of magnitude) and good statistical confidence by scaling multiple negatives. Imaging plates are also very effective for quantitation

due to very high dynamic range (between 16 and 20 bits, or roughly 10^5) (Zukhlistov et al. 2004).

Recently, charge-coupled devices (CCDs) have been coming to the forefront as the preferred image acquisition tool. The effective dynamic range from CCDs is not particularly large due to shot noise; additionally, they are delicate and expensive, but their convenience hugely outweighs their disadvantages. CCDs typically have 12-14 bit dynamic range, and the low 2-4 bits are obscured by noise — the effective dynamic range is thus $\approx 10^3$ for CCDs. The dynamic range can be increased by broadening the spot profiles slightly (also applicable to the other parallel detection techniques listed above). This can be accomplished by converging the beam or changing diffraction spot focus. This allows longer exposure times by increasing the intensity measurable before pixel saturation. A caveat is that broadening the peaks can cause weak reflections to fall below the noise floor preventing their measurement, so a careful optimization is desired.

The measurement technique that yields the highest dynamic range is the diffractometer method (Bagdik'ianc and Alexeev 1959; Avilov et al. 1999). In this scheme, the diffraction pattern is shifted serially using the image deflectors such that electrons are collected sequentially for each spot into a Faraday cup. The dynamic range is dependent upon how long the intensities are integrated. A drawback is that it is a serial technique, hence the acquisition takes a long time, especially if high dynamic range is needed. Additionally, the Faraday cup aperture is fixed in size, hence care must be taken to avoid quantifying multiple spots simultaneously especially in the case of large cell structures. Often this can be avoided by increasing camera length, though diffuse background effects cannot be eliminated (in any case, they are reduced by precession).

Ultimately, it may not be possible to install a PED system in many microscopes because of administrative issues. The service warranty is a very important factor: not all manufacturers are supportive of modifications to their instruments so this issue must be handled with care.

To summarize, the key practical requirements for implementation of precession:

- The precessed incident beam must yield a symmetric cone of incident directions about the crystal zone axis;
- The de-scan must bring the diffracted beams together to form uniform points (or non-overlapping discs in the case of beam convergence) for accurate measurement;
- If spatial accuracy is desired in the experiment (e.g., fine-grained polycrystalline specimens), the conical probe fulcrum must intersect the specimen precisely in 3-dimensional space;
- A detector must be able to acquire the integrated intensities at sufficient dynamic range for quantitation;
- The manufacturer must continue to support the microscope with a moderately invasive accessory attached.

2.3. Aberration Analysis

While the precession mode can be readily implemented on a variety of instruments, ultimate performance is limited by the classic problem of objective lens (OL) aberrations. The primary difficulty in implementing electron precession on conventional instruments lies in the objective's inability to accurately focus high angle rays onto a precise region of the specimen, and to release the diffracted beams in trajectories that precisely describe the diffraction vectors with respect to the incident radiation. Aberrations throughout the optical system adversely affect the ray trajectories, resulting in a delocalized hollow cone probe fulcrum at the specimen and poorly converging diffraction points at the diffraction plane.

Figure 2.4 is a cartoon of a modern condenser-objective instrument showing the ray paths traversed by a precessed transmitted beam. It demonstrates in more detail the role of the objective lens in PED. The convergence point at the specimen should ideally be as small as possible to reduce the chance of illuminating a specimen defect and to minimize the variation in sample thickness and orientation. Aberrations are inherent in all cylindrically symmetric round lenses (Scherzer 1936), therefore the ray path of the incident beam will necessarily deviate from ideal as the incident beam precesses azimuthally through the objective lens field. This may cause the probe to wander in the image (specimen) plane during precession. Highest performance is obtained when the alignment is optimized to minimize this wandering effect.

An idea of minimum probe size that can be obtained is available by studying the behavior of convergent probes. In conventional microdiffraction, the diameter d (containing 70% of the intensity) of a filled convergent probe is dominated by the spherical aberration coefficient C_s, and is described by the following relation:

$$d_{70\%} = 0.66\lambda^{3/4}C_s^{1/4}, \tag{2.6}$$

where λ is the electron wavelength (Spence and Zuo 1992). In equation 2.6, the defocus has been optimized to yield the smallest probe. This puts strict constraints upon precession: the smallest probe size is obtained when C_s is minimized and when the defocus term is smaller than the spherical aberration term. Minimum C_s is obtained at a specific known lens excitation (in Amperes) that is measured at the factory and is different for every lens. Therefore, to obtain the finest probe, the defocus must be tuned not by the OL excitation, which is fixed, but by the specimen height z (i.e., it must be tuned mechanically). At the start of alignment, the specimen must therefore be at the eucentric height ($\Delta z = 0$) which is usually the expected crossover.[1] The unaligned condition yields a circle only if non-spherical aberration terms are small (as indicated in figure 2.4 and 2.5); ellipses or polygons/stars result if the non-spherical terms are large. Figure 2.5 shows a case where the three-fold aberration is prominent. After alignment, the lobes in the image were brought down to a disc approximately 25 nm in diameter.

[1]Eucentric height is formally defined as the height of the specimen at which its image does not move laterally as a function of specimen tilt.

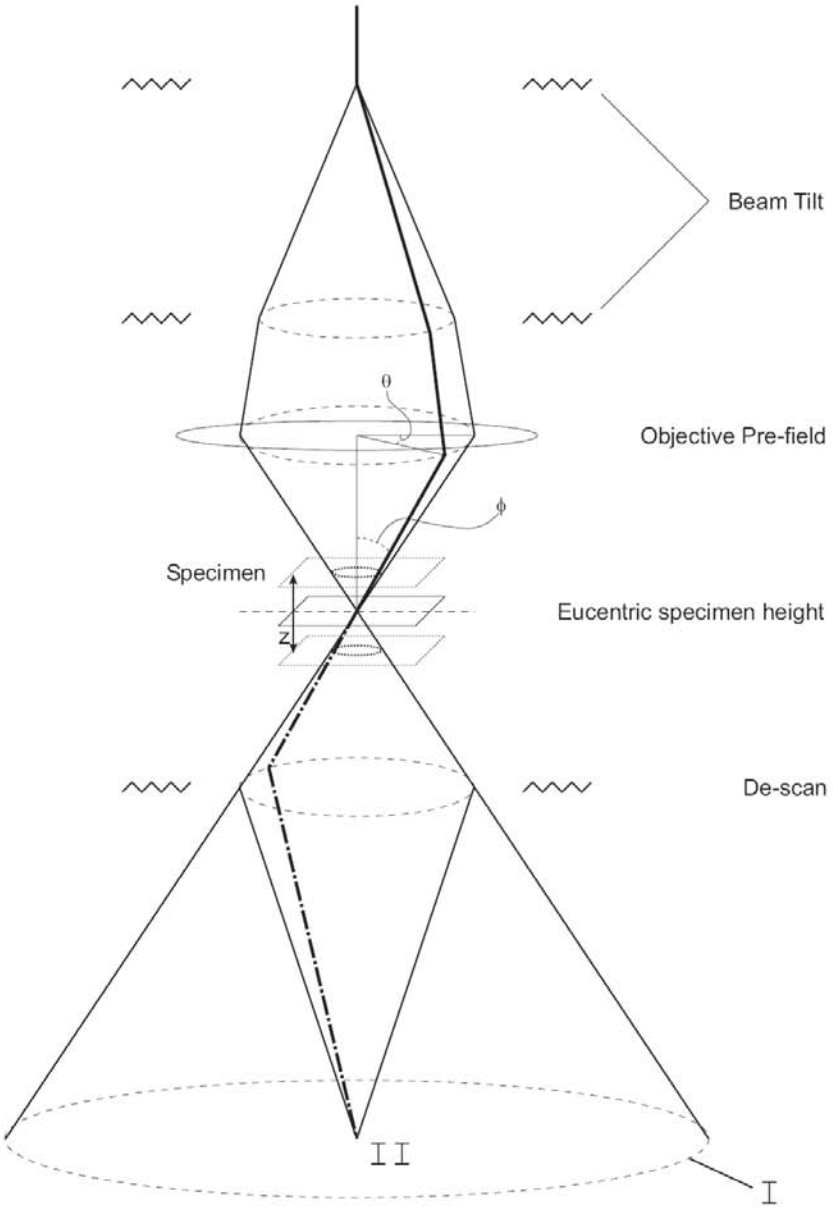

Figure 2.4. Precession geometry in a modern condenser-objective TEM with double deflection coil system showing the path of the precessed transmitted beam. The objective prefield acts as an additional condenser lens. Circle I is generated by the beam tilt scan. De-scan collapses circle I down to point II.

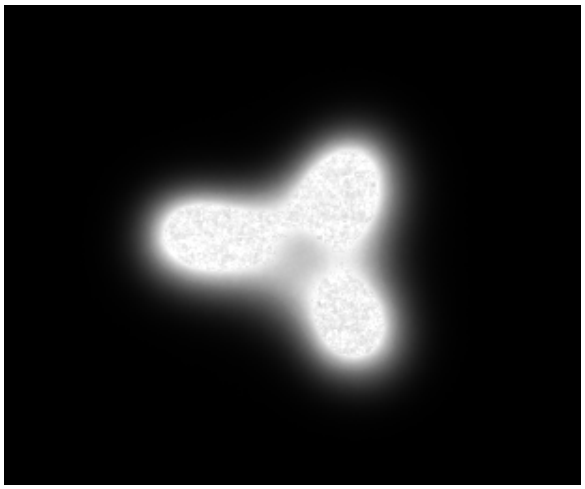

Figure 2.5. Star of merced, formed by the unoptimized precession probe prior to full alignment. The three-fold astigmatism term is dominant. Each lobe is roughly 25 nm. The image was taken on a JEOL 2000FX retrofitted for precession.

Before going into the details of the aberrations, it is relevant to mention field emission electron sources. They have higher brightness than thermionic sources and, additionally, the radiation emitted is extremely coherent (the field emission gun is the electron optic analog of the laser). When a field emission source is used with the Koehler mode of illumination — a mode where the illumination aperture is conjugate with the sample — a highly coherent small probe results with very parallel illumination. This mode, called nano-beam diffraction (NBD), is the mode in which the latest precession system installed in the JEOL 3000F is typically operated.

PED involves much larger angles than the conventional probe convergence angle of micro- and nano-diffraction, hence higher order aberrations and their effects should be considered.[2] The aberration function is described by radial and axial components in the x-y plane in the Krivanek notation, a convenient form for precession (Krivanek et al. 1999). The following aberration function is expanded to fourth order in this notation:

[2]This discussion excludes diffraction ronchigrams, which are often used for probing and tuning aberrations in aberration-corrective systems. The convergence angle in ronchigrams is often hundreds of mrad.

$$
\begin{aligned}
\chi(\rho,\theta) &= \rho(C_{01a}\cos(\theta) + C_{01b}\sin(\theta)) \\
&\quad + \frac{\rho^2}{2}(C_{10} + C_{12a}\cos(2\theta) + C_{12b}\sin(2\theta)) \\
&\quad + \frac{\rho^3}{3}(C_{23a}\cos(3\theta) + C_{23b}\sin(3\theta) + C_{21a}\cos(\theta) + C_{21b}\sin(\theta)) \\
&\quad + \frac{\rho^4}{4}(C_{30} + C_{34a}\cos(4\theta) + C_{34b}\sin(4\theta) + C_{32a}\cos(2\theta) + C_{32b}sin(2\theta)) \\
&\quad + \frac{\rho^5}{5}(C_{45a}\cos(5\theta) + C_{45b}\sin(5\theta) + C_{43a}\cos(3\theta) + C_{43b}\sin(3\theta) \\
&\quad + C_{41a}\cos(\theta) + C_{41b}\sin(\theta)). \qquad (2.7)
\end{aligned}
$$

χ describes the distance between the aberrated wavefront and the Gaussian wavefront along the aberrated ray (see figure 2.6); a ray intersecting the aberration function at a point (ρ,θ) will be subjected to a deviation described by a polynomial radially and a harmonic function azimuthally. For precession, we are interested in illuminating the lens in an annulus whose radius is considerably beyond the limits of conventional TEM imaging. The minimum desired ϕ is on the order of 20 mrad, and benefits continue to occur past 50 mrad. In real space, the aberration function produces a deviation from the Gaussian focal point (wandering probe), and in reciprocal space, a deviation in the ray's incidence angle. In practice either is easy to optimize by itself; however, correcting one without compromising the other is the major challenge in aligning a precession system. Consistency of the cone illumination semi-angle has proven to be a relatively loose constraint ($\pm$1 mrad is sufficient, see section 3.1) so real space localization can be considered the primary optimization constraint.

It has already been mentioned that spherical aberration can be roughly compensated for by a simple defocus adjustment, or more preferably by a shift in specimen height to preserve optimal excitation of the objective. In conventional microscopes, the next limiting aberration after C_s is three-fold astigmatism (Krivanek and Stadelmann 1995). Two-fold is present but can be relatively easily corrected by the objective stigmators. The coefficients of largest concern in the context of equation 2.7 are three-fold astigmatism (C_{23a} and C_{23b}) and two-fold astigmatism (C_{12a} and C_{12b}), illustrated in figure 2.7.

Beam tilt purity and the two-fold OL stigmators can compensate for most of C_{12}, however sometimes C_{23} is left over and must be corrected dynamically during scan alignment. In the precession implementations given in the appendices, additional two-fold and three-fold compensations are made in the conical scan in conjunction with tilt purity adjustments to achieve a suitable compromise between incident ray direction in reciprocal space and real space convergence. The practical limits have been about 40-50 mrad in the JEOL instrument. Above this threshold we have found a combination of higher-order objective aberrations and projector distortions to dominate.

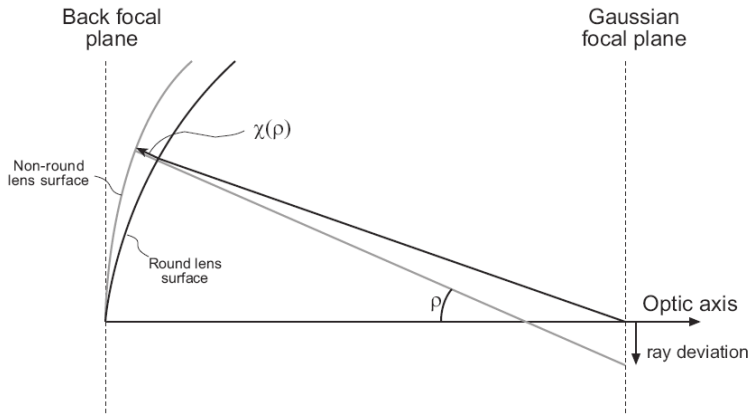

Figure 2.6. The aberration function $\chi(\rho)$ describes the deviation from the ideal round lens along the projected direction of the aberrated ray. The aberrated ray deviates in angle from ideal by ρ; in real space this corresponds to a deviation of probe location (the origin of probe 'wandering').

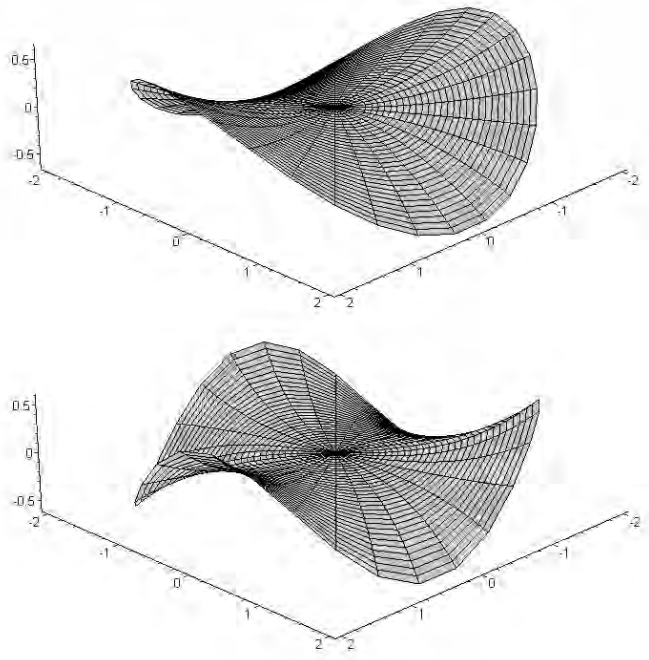

Figure 2.7. a) Two-fold (potato chip) and b) three-fold (monkey's saddle) aberration functions (arbitrary units). These are the primary aberrations that require compensation in conventional instruments.

Aberration-corrected instruments are particularly suitable for the precession mode. Scan systems with several degrees of freedom are by default incorporated into the latest instruments and are well-suited for providing the deflections for conical illumination. The latest generation correctors can provide up to about 70 mrad cone semiangle without geometric compensation in the scan, thus a simple circular deflection path described by the scan system will yield optimal conditions for the experiment. Especially advantageous is the fact that experiments can be executed at various ϕ with single-variable adjustment allowing quick experiment setup and enabling non-conical experimental geometries (potentially useful as alternative modes of precession) that would otherwise be impossible to generate without a comprehensive aberration model of the microscope column.

In such instruments the primary aberrations are higher-order. Beyond the flat phase patch, the aberration function increases rapidly (e.g., correction to C_5 in the latest Nion Co. corrector produces an aberration function increasing to the 6^{th} power with angle). An attempt to extend the precession semi-angle to very high values (> 75 mrad) will yield rapidly diminishing returns. However, geometric compensation similar to that used on the Northwestern implementations utilizing an N-fold function, where $N - 1$ is the corrector order, should nevertheless yield beneficial results.

The de-scan section of the precession instrument collects diffracted beams from each tilt condition into discrete integrated spots suitable for quantitation. This collection must happen somewhere between the image plane and back focal plane. The constraints are different from the beam tilt because the symmetry about the specimen is broken (except in the case where immediately post-specimen deflectors are available). Since precession involves angles considerably larger than those in conventional diffraction patterns, and angles become larger as the diffracted beams travel down the column, deflectors must be capable of larger deflections. The high angles involved also subject the diffracted beams to distortion in the intermediary lenses (astigmatism) in addition to projector lens distortion (astigmatism, pincushion/barrel, and spiral).

The de-scan should ideally be executed immediately post-specimen to avoid these effects. The second choice is in the intermediary optics before the diffraction pattern is formed. Sometimes this is not possible because the intermediate alignment deflectors are too feeble. The last resort is the imaging deflector: almost all conventional instruments incorporate a user-accessible deflector located just above the projector lens. Newer instruments are incorporating more post-specimen deflection coils finding suitable de-scan coils should less likely be an issue in modern instruments.

2.3.1. The Future

The ability to tailor the aberrated wavefront extends naturally to an ultra-high-angle dynamically correcting scheme, suggested by N. Dellby of Nion Co. Since the precession is executed in discrete steps and the incident beam typically has small convergence (<5 mRad), the correction system can extend the hollow probe performance in a given angular direction by compromising

the central disc of flat phase and shifting it off of the lens axis. The aberration function of figure 2.8 demonstrates this principle.

The aberration function contains a mixture of C_{10}, C_{12a}, C_{30} (or C_s), and C_{45a} to create an extended flat phase patch that could in practice be scanned around the lens axis by altering the aberration coefficients dynamically. Similarly, a rotationally symmetric ridge function (muffin tin form) could be generated - effectively a combination of defocus, C_s, and C_5 - creating a flat phase annulus that, while not focusing rays to the Gaussian plane, is nevertheless suitable for high-angle conical precession. This would extend the usable convergence angle to beyond 100 mrad while maintaining a static set of aberration coefficients, yielding excellent stability and higher angles than those achievable with an instrument corrected to be aberration-free.

2.4. Review of Previous Instruments

The earliest precession instrument was reported by Vincent and Midgley in 1994 and was based on a Philips EM430 operating at 300 kV. A Wien bridge oscillator provided the precession scan signals; frequency was capped at 30 Hz to prevent distortions due to deflector bandwidth limitations. The stock instrument included inputs for beam tilt, however the de-scan circuitry did not support external control. Therefore, the de-scan controls were completely replaced by the analog oscillator.

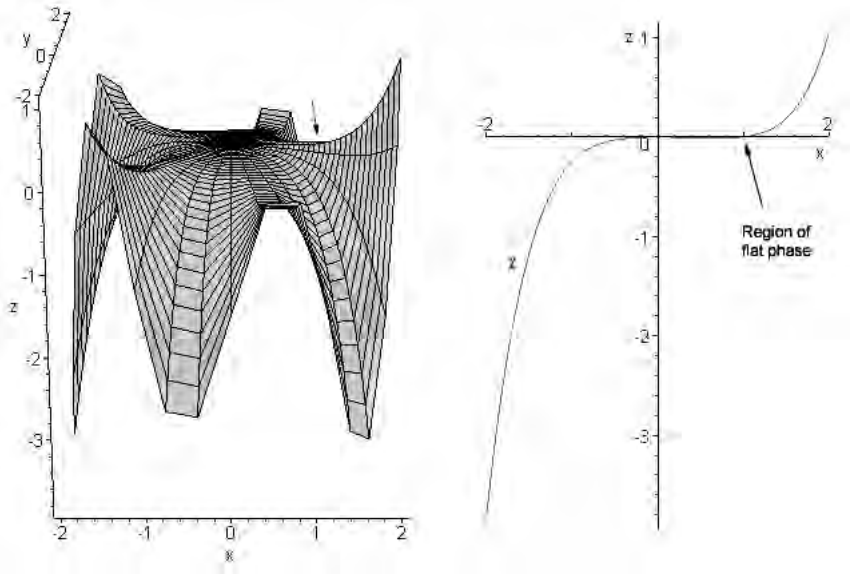

Figure 2.8. An aberration function containing coefficients C_{10}, C_{12a}, C_{30}, and C_{45a} (mixed in a respective ratio of 1:2:3:3). The effective aberration surface has rough 5-fold symmetry. In the x-z section on the right, an odd-order function describes a region of flat phase extended in the $+x$ direction indicated by the arrows.

This early instrument was reported to theoretically yield better than a 10nm diameter probe in convergent illumination mode, however in practice it gave a 100nm probe due to probe-wandering caused by aberrations. The feasible tilt range was reported at 8° (≈ 140 mRad), however the earliest experiments were conducted below 25mRad and later experiments on Al_mFe using more parallel illumination had 16-40 mrad semiangle. Both of these figures are more consistent with the < 50 mrad figure we have found typical for this type of optical distortion-limited system. Projector lens distortion was the primary limiting factor causing errors in the de-scan at moderate angles that complicated automated measurement.

Gemmi has developed a precession instrument on a 300 kV Philips CM30T chassis that operates at 35 Hz (Gemmi 2001). The sinusoidal signals were generated in an outboard analog oscillator and fed into the external interface. The signals were digitized by the interface and outputted to the scan coils in analog form by the microscope CPU. This A-D-A process is active only in the selected-area channeling-pattern operating mode (part of STEM mode on the CM30T). Nanobeam illumination mode was used, which is the Koehler equivalent on this instrument (parallel illumination). One of the limitations of this type of system is that signal quality at the coils is limited by sampling rate and A-to-D converter precision at the input, and at the output by the D-to-A's (DACs) supplying the coil drivers. Due to this uncertainty, some difficulty with de-scan precision in early revisions was reported that appears to have later been resolved (Gemmi et al. 2003).

The study by Gemmi et al. (2003) on Ti_2P generated a three-dimensional dataset merged from several zone axis patterns collected on the CM30T. In this study, the device was operated with parallel illumination, forming sharp spots. A moderate tilt angle of 17 mRad was reported, limited by distortions in the optics, and the probe size on the specimen was approximately 100 nm.

The early studies demonstrated PED's potential as a crystallography tool, however, optical distortions clearly limited both instruments' performance and affected the results. The next section demonstrates an approach using simple geometric distortion compensations that enhance PED data quality and improve the alignment speed and reproducibility of precession experiments.

2.5. Design Approach

The design approach described in this chapter has been applied to two different microscope systems. The first embodiment was based upon the Hitachi UHV H-9000 microscope (see appendix B for details). On that instrument, the aberration compensations were essential but proved to be insufficient for high-precision precession due to the fact that manual specimen z-height adjustment was not available on this microscope, and the specimen was almost never inserted into the microscope near the eucentric height. Better design and careful refinement of alignment procedure yielded very good performance and high reliability for a second system based upon the JEOL 2000FX (appendix C). The hardware for the second system has since been moved onto a JEOL 3000F field-emission microscope, where minor modifications have

been applied to further improve performance. An overview of the system design is presented in figure 2.9.

Beam deflection above the specimen with complementary synchronous de-scan below can be produced in most instruments using the beam tilt coils and the projector image shifts. This can be accomplished by supplying the appropriate scan signals directly to the analog coil driver circuits. We aimed to provide a simple and straightforward human-machine interface to control precession hardware that has been designed for stability and reliability. It is intended to work within the framework of the existing system without affecting any original functionality.

2.5.1. Stock Instrument Hardware

Deflection systems inside common TEMs follow a general theme wherein a control voltage is supplied to a current amplifier that drives current in a coil (figure 2.10). In such systems, control voltages are typically under 10 volts, and currents in the coils do not exceed one or two amperes. The preamplifier shown in the schematic is often configured to sum several signals (two in figure 2.10), so it will also also be referred to as a summing junction (SJ).

Microscopes are used primarily for steady-state operation (scanning microscopes excluded), therefore coil drivers in many microscopes have been designed for DC operation and stability.

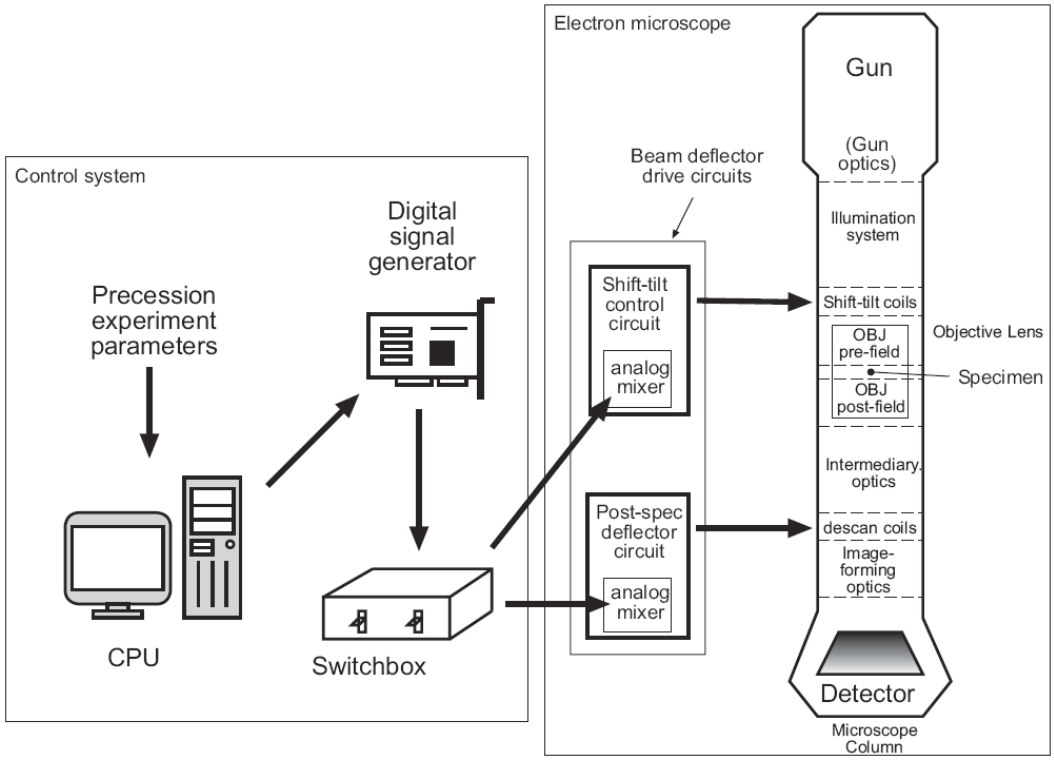

Figure 2.9. Overview diagram of the precession system.

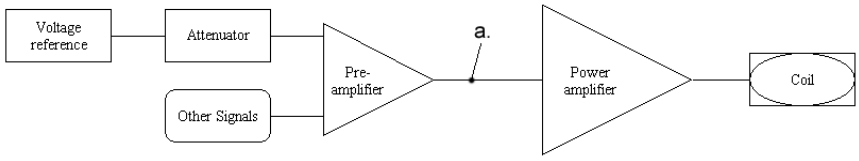

Figure 2.10. Generic amplifier for driving an electromagnetic coil.

Consequently, they will not have the bandwidth to support precession in many cases. This generates major problems for a PED retrofit, which needs a slew rate on the order of a 1000 V/s (several hundred Hz at full amplitude) with low distortion. While the coils can usually support operation in the KHz regime, the coil drivers often do not have the necessary bandwidth, especially in older instruments. Coil drivers are typically bipolar, meaning they amplify both negative and positive signals. A typical driver stage is made up of a preamplifier stage followed by voltage-to-current amplifier whose output devices comprise a pair of power transistors operating in push-pull configuration (see appendix B for a sample circuit). When fed a bipolar signal that is too fast for it to track, the output stage will respond too slowly when crossing the zero voltage point of the waveform, generating distortion. This arises because a transistor exhibits a non-zero time delay between the application of signal to the gate and the start of current flow from source to drain. In precession, this will result in a kinked "pinwheel" pattern in the scanned beam. The effect is called crossover distortion or "the class B problem," and the effects on the waveform and scanned beam are shown in figure 2.11.

The solution to crossover distortion is to either bias the output transistors so that they never turn off (e.g., always conducting current) or switch to faster output transistors. A simple coil driver stage based on power operational amplifiers is provided in the Hitachi example to demonstrate a solution to this problem (appendix B).

Most deflection coils are dipoles, meaning two windings are used to deflect the beam in orthogonal directions within a plane perpendicular to the optic axis. Identification of the axes in each coil is key since rotations or opposing field polarities often exist between deflectors throughout the column; this knowledge will prevent mismatch of precession direction between scan and de-scan and give an idea of the phase shift between the coil sets that must be applied when the system is aligned.

2.5.2. Circuit Modifications

The precession signal can be conveniently inserted at any point in the circuit where the signal is in voltage form and low in amplitude (a few volts). An example is between the pre- and power amplifer at point **a** in figure 2.10, where a small amplifier module can be inserted in series to combine the scan signal with microscope console commands. Alternatively, if summing junctions are preferred, the preamplifier can be configured in summing mode and the signal can be added as an extra input to the preamplifier. Simple circuit building blocks based on operational

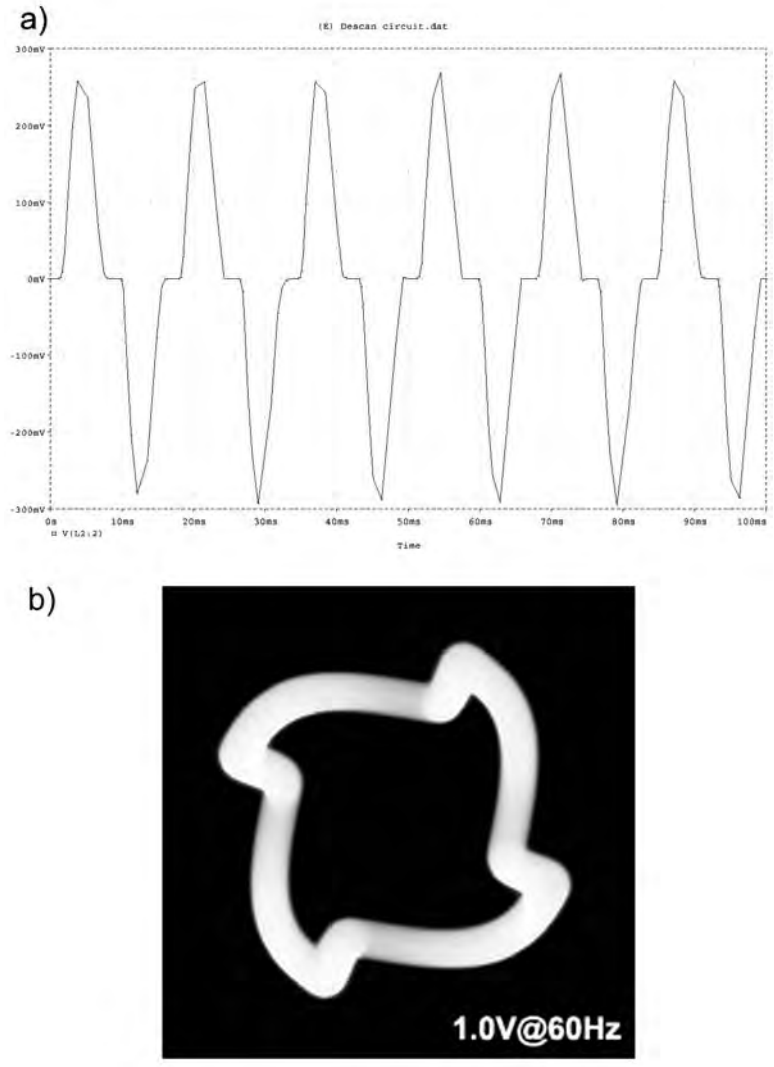

Figure 2.11. a) Simulated waveform for the H-9000 bipolar push-pull DS amplifier demonstrating crossover distortion. At each zero-crossing point, there is a plateau in the waveform. b) A precessed beam tilt pattern demonstrates how this distortion manifests in the pattern: since x and y coils are out of phase by 90 a pinwheel pattern is generated.

amplifiers (op-amps) are very suitable for this purpose; op-amps are easy to use due to compact and simple physical circuit layout, and have high intrinsic power supply rejection ratio (e.g., a variety of supplies can be used, including unregulated types). A section on operational amplifier use is supplied in appendix A.

The first two precession implementations used add-on mixer modules placed in series on low-level signal lines. Custom modules were used for reasons of versatility, listed here:

- When they were initially designed, it was not certain whether the input impedance of the stock circuit was sufficient for application of external signals. High impedance op-amps could be used.
- It was thought that several auxiliary signals might be added in the future. A circuit board had several quick-release inputs for future expansion.
- In some cases, the signal may need to be scaled above the output range of the scan signal source, or scaled down to increase the effective resolution of the source. Individual gain settings could be easily set by altering input resistor values.

Figure 2.12 shows the mixer-buffer module used in both implementations described in this paper, comprising a single-ended inverting mixing amplifier (SJ) followed by an inverting buffer stage that corrects polarity and isolates the SJ from downstream electronics. One amplifier circuit is used for each input (four total), and the gain of each external input can be altered by changing the value of the input resistor for V_{prec}. A 15V split supply was used, and appropriate bypassing was used to enhance amplifier performance. The 3.3nF feedback capacitor in the mixer stage limits the bandwidth to about 5KHz in the case that downstream components are sensitive to the high-frequency components from the signal generator's non-oversampling DAC. A low-distortion part (e.g., film-type) is preferred for this application.

It is relevant to note that while beam tilt is controlled by two inputs at the console, 4 or 6 independent windings in a stacked coil pair work in combination to provide the tilts. Many microscopes allow high-level beam tilt control from just two analog signals because shift-tilt alignment has traditionally been executed in analog circuitry; the precession scheme presented here applies to this type of microscope. Modern digital microscopes now more commonly accomplish shift-tilt alignment in the digital domain, hence there may not be a location to

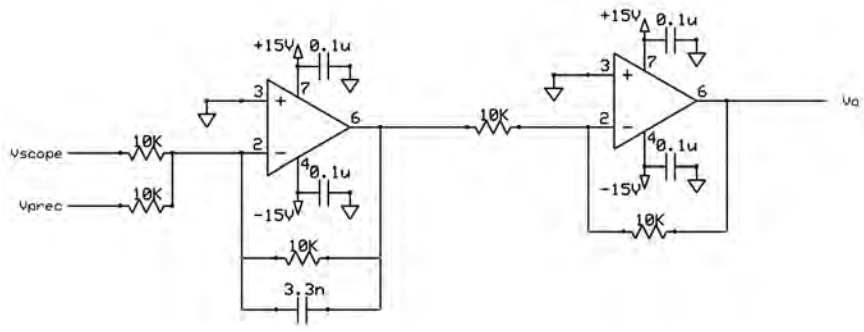

Figure 2.12. Mixer-buffer circuit used to add precession capabilities to a deflector amplifier. The first stage sums the normal microscope signal with the precession scan signal and is followed by an inverting buffer stage that corrects phase and isolates the mixer from downstream components. This circuit can be installed at point *a* in figure 2.10.

insert the two beam tilt signals. The solution would either require using the external interface (A-D-A process) or, more desirably, require low-level modification of individual coil drivers (e.g., extra scan inputs) and additional programming to accomplish shift-tilt alignment and ultimately conical illumination.

2.5.3. PC Hardware

A PCI-671x series data acquisition and control (DAQ) board by National Instruments was chosen for the Northwestern systems. This board employs 12-bit DACs (sufficient resolution for precession) to generate signals in the range of ± 5 V. Depending on the microscope, the gain on this input signal may need adjustment to match the signal levels inside the microscope. The PCI-671x's main strength is on-board cyclic buffering which allows a fast non-CPU-limited output rate. The standard operation rate is 60-120 cycles per second with an angular resolution of better than 1° (> 360 tilts); for four combined channels, this is under 0.1 megasamples per second and is well within the 1 MS/s limit for this board. The rate is chosen to synchronize to the AC mains frequency to prevent beat frequency artifacts from showing up in the scan (an example is given in appendix C). Larger angles require higher resolution and correspondingly higher output rates, so for $\phi > 30$ mrad, 0.5° angular resolution is often used. DAQ boards from other vendors may be equally suitable and can offer higher performance, and if higher resolution is needed, the PCI-673x from NI offers 16 bits of resolution.

A primary concern with PC-based systems is inherently dirty ground due to switching power supplies and digital circuitry. In general, the PC's ground reference should be bridged to the microscope near the relevant signal circuitry but placed at a common point that offers stiff earthing. Additionally, long runs of cable should be shielded to prevent external fields from modulating the signal. To prevent ground loops, the shield should be connected to ground only at one end of the interconnections (preferably at the source). For microscopes that require very high stabilities, differential scan signals should be utilized to prevent noise from entering the microscope.

2.5.4. Software

The scan generator provides four computer-generated sinusoidal signals calculated by a software routine. Deflection coordinates for each point in the conical scan are calculated, sent to the hardware buffer, and the subsequent waveforms are outputted 90° out of phase to describe a circle of deflection points where the phase difference polarity defines the direction of rotation in each deflector plane. Aberrations in the objective lens can be compensated for by adjusting deflection coordinates in the BT scan to counteract the effect of the aberration contours in the lens. The DS coil deflections are applied in the direction opposite to the tilt to bring the circle generated by BT scan down to a point in the diffraction plane (point II vs. circle I in figure 2.4). The DS signal is phase shifted with respect to the BT scan by a fixed value ϕ_{DS} in the azimuthal plane.

The DS controls can be used to circumvent distortions in the projector deflectors and lens, or to remove the effect of small residual aberrations not eliminated by the BT. With care, the integrated intensities can be brought down to measurable spots a fraction of a milliradian in diameter. Small errors in BT can be readily compensated by careful de-scan alignment even when moderate to large ϕ is used (> 25 mRad).

While astigmatism in magnetic lenses is described by hyperbolic functions, approximate two-fold and three-fold functions are sufficient for their compensation. The software algorithms that generate these compensations are based upon the following set of relations:

$$x_1 = A_1 \cos\theta; \tag{2.8}$$

$$y_1 = A_1 \sin\theta; \tag{2.9}$$

$$x_2 = s \cos\theta; \tag{2.10}$$

$$y_2 = -s \sin\theta; \tag{2.11}$$

$$x_3 = [A_3 \cos 3(\theta + \phi_3)] \cos\theta; \tag{2.12}$$

$$y_3 = [A_3 \cos 3(\theta + \phi_3)] \sin\theta; \tag{2.13}$$

$$x_{out} = [(x_1 + x_2)\cos\phi_2 + (y_1 + y_2)\sin\phi_2] + x_3; \tag{2.14}$$

$$y_{out} = [-(x_1 + x_2)\sin\phi_2 + (y_1 + y_2)\sin\phi_2] + y_3. \tag{2.15}$$

The functions x_1 and y_1 represent the basic oscillatory functions that produce the precessed circle as θ traverses 2π radians. Functions x_2, y_2, x_3, and y_3 are used to generate two- and three-fold compensations, where the variable s is a scaling factor for the two-fold elliptical function related to the base deflection amplitude (cone semi-angle ϕ), and ϕ_2 and ϕ_3 are phase shifts that rotate these two- and three-fold compensation functions in the azimuthal plane. These constituents yield the functions x_{out} and y_{out}, which contain various pre-field correction amplitudes in addition to the conical precession scan. In practice, the correction magnitude is on the order of 1% of the base deflection amplitude A_1.

The software interface comprises BT amplitude controls, the two-fold and three-fold compensations described above, and phase shift ϕ_{DS} between BT and DS scans. The amplitude and two-fold functions are mirrored for the descan. Additionally, the software allows control of the precession rate and precise tuning of frequency and angular resolution. The interface, based on LabView visual language, is shown in figure 2.13.

Lens distortions in the lower column can complicate intensity quantification at higher α. If the de-scan is done at the projector, the quality of precessed diffraction spots is highly dependent upon cone semi-angle. The spot uniformity deteriorates with increasing ϕ and diffraction spot centers become displaced in the diffraction plane due to projector distortions (figure 2.14). This was a limitation on the EM430 on which the first precession instrument was based. For some microscopes, the maximum possible tilt may be restricted by objective lens aberrations before post-specimen distortions become a limiting factor.

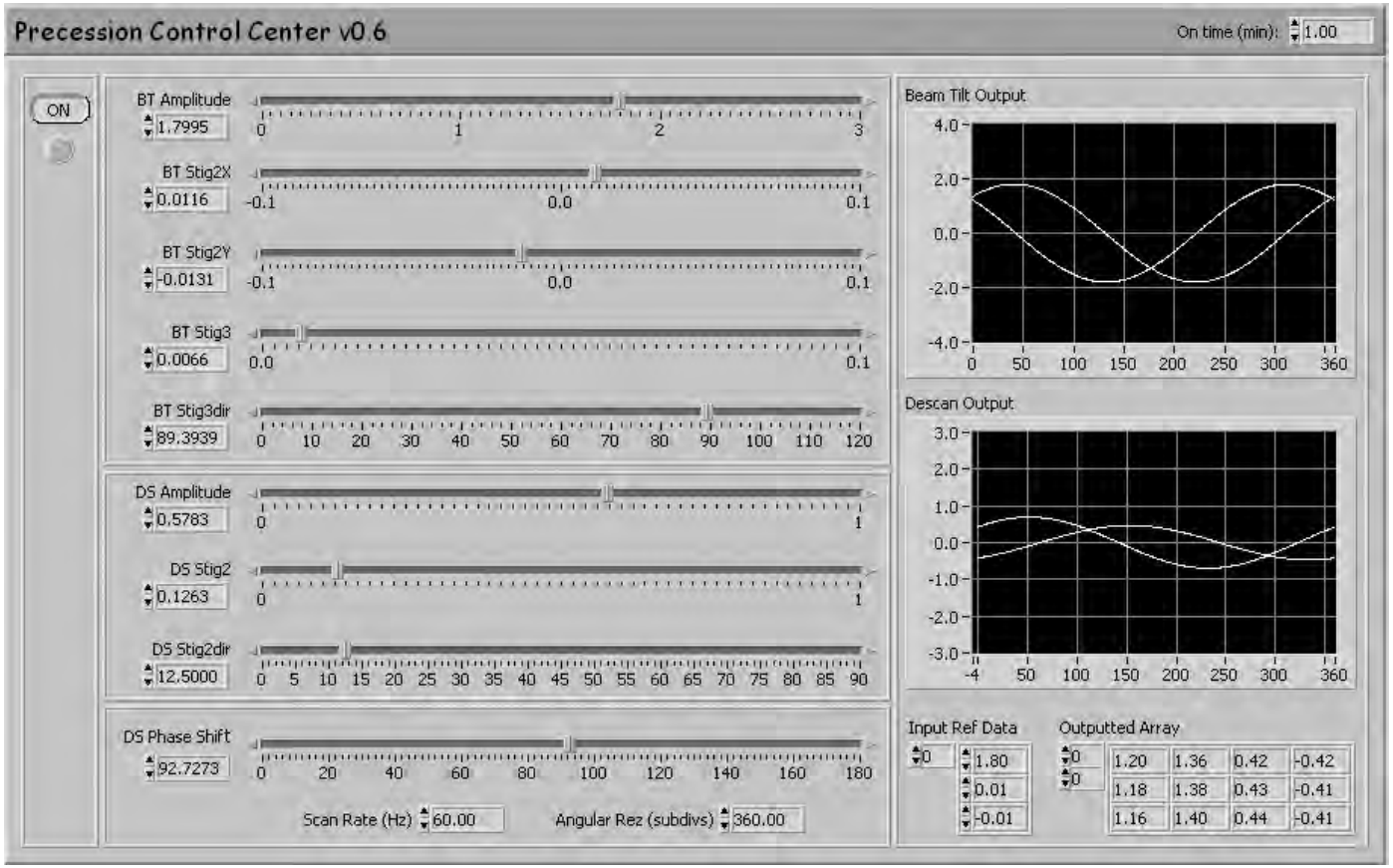

Figure 2.13. Precession software interface.

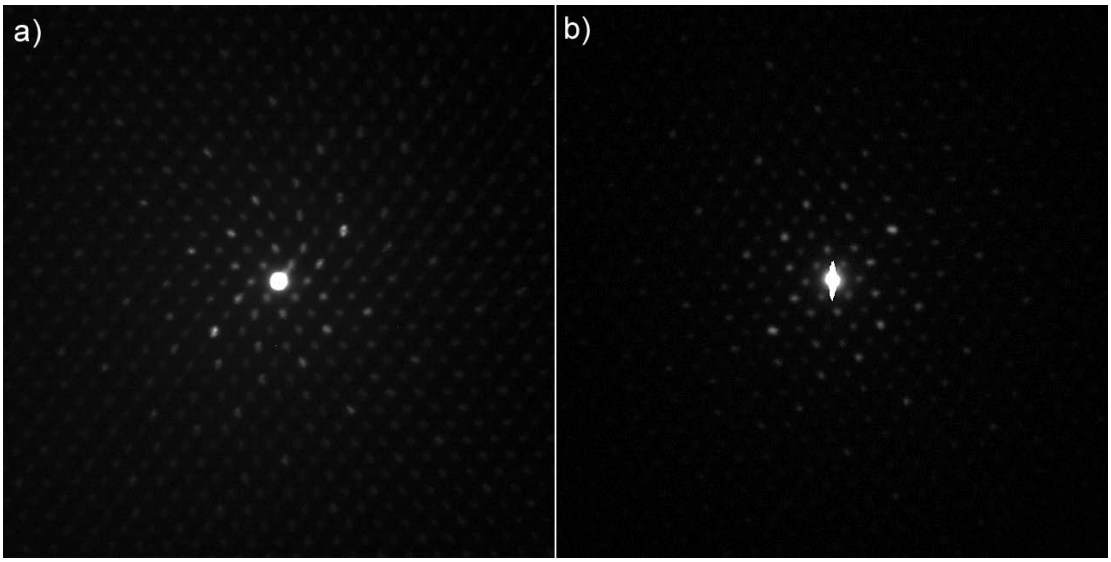

Figure 2.14. Precession patterns for 60 mrad cone semiangle (a) and 40 mrad cone semiangle (b). Spiral distortions in the projector lens alter the shape of the spots and shifts their position, preventing straightforward intensity measurement. Using a smaller cone semi-angle gives an improved and easier to measure spot pattern.

A number of modern instruments have incorporated post-specimen deflectors that mirror the scan coils prior to the specimen. This is very advantageous for PED, so we include here some guidelines for implementing shift-tilt alignment in software. The common scan coil arrangement uses two deflector pairs, which usually have their axes relatively aligned in the column. Four inputs are necessary for the scan, and another four are necessary if the de-scan has the same type of configuration. The deflectors will behave linearly with input current throughout most of their range, however for large scan angles, the brightness centering (shift) should be zeroed to avoid hitting nonlinearities asymmetrically as ϕ increases. The shifts can be zeroed via the spot size alignment feature on many microscopes. Shift-tilt purity can be accomplished by applying a simple linear combination of the tilt inputs:

$$x_u = Ax_t; \tag{2.16}$$

$$y_u = By_t; \tag{2.17}$$

$$x_l = x_t + Cy_t; \tag{2.18}$$

$$y_l = y_t + Dx_t. \tag{2.19}$$

The variables x_t and y_t denote the tilt signals sent from the precession system (or microscope), and x_u, y_u, x_l, and y_l correspond to the upper deflector pair and lower deflector pair, respectively. The four coefficients A, B, C, and D correspond to the shift-tilt purity controls

available on most microscopes. These are used for the "wobbler" alignment; precession performs a similar operation, but it probes aberration space isotropically so it can provide an even better alignment than the wobbler. Many azimuthal phase shifts are present along the beam path, since at least 4 deflector coils with 8 individual windings will be active, so 16 bits of resolution in the signal generator is recommended to ensure alignment. The recently-released commercial precession system called SpinningStar from NanoMegas Corp. uses this scheme in pre- and post-specimen deflectors. This allows free scaling of the tilt amplitude without compromising the alignment, so in this case the de-scan amplitude would be dependent upon the scan amplitude variable.

2.5.5. Conclusions

The key aim for this design approach has been to balance function, usability, and complexity. By utilizing graphical-tool-based object-oriented software to control the digital electronics, the system preserves the intuitive analog feel of a stock instrument yet is not limited by the inflexibility and inherent design complexity of a fully analog system. With distortion compensation, the precession pattern quality improves dramatically, and images can be digitized readily by automated cross-correlation methods (appendix F).

The example systems in the appendices show that retrofit of precession mode onto conventional instruments is not difficult, and (perhaps more importantly) that a high-performance implementation can be very inexpensive. The systems described each required less than US$2,000 in parts costs. Excellent results can be expected if the most important requirements are met, namely compensation of aberrations, manual z-height correction, and careful user alignment.

Before concluding this chapter, it must be mentioned that in the progress of conducting the work presented here, not only were important instrumentation parameters elucidated, it was also discovered that it is sometimes much easier to install PED capability on older analog instruments. This has extremely important ramifications in the field. While fancy instruments such as aberration corrected microscopes with sophisticated detectors make PED work better, all that is necessary is a microscope that has well-implemented shift-tilt purity controls with sufficient range, a pair of post-specimen deflectors, and an electron film magazine. The resolution extension by a factor of 100 granted by PED promises new life to old instruments. Currently, a huge installed base of thousands of TEMs incapable of atomic-resolution imaging exists that would directly benefit from this type of retrofit. In many cases, the costs for a commercial precession retrofit would prove a factor of 5 or 10 smaller than the cost for full replacement of the instrument.

In the next two chapters, the precession system shall be put to use in an investigation of real materials. The care put into ensuring precise and reproducible measurements by the instrumentation will be readily apparent in the quality of the recovered data and the results they generate.